A Non-rigid Polygon Registration Framework and its Application to Enhancing Building Footprint Accuracy using Aerial LiDAR

Amine Boussik[1], Nicolas Girard[2], Liuyun Duan[2], Bruno Vallet[1]

[1] Geodata Paris, IGN, LASTIG, F-94160 Saint-Mandé, France.
(amine.boussik, bruno.vallet)@ign.fr

[2] LuxCarta Technology, Mouans-Sartoux, France.
(ngirard, lyduan)@luxcarta.com

Keywords: Rigid registration, Non-rigid registration, Building footprints, LiDAR data, Cadastral datasets, Urban mapping

Abstract

Accurately registering building footprints from heterogeneous datasets with LiDAR data remains a critical challenge in urban mapping and 3D reconstruction. The objective of this work is to register source data, defined as 2D cadastral vector footprints from structured, regularized, or manually-verified datasets to target building footprints derived from classified aerial LiDAR. LiDAR provides direct 3D information with precise footprint positioning and high spatial resolution, enabling a geometrically reliable representation of dense 3D structures. Conversely, source datasets are not always up-to-date, and may exhibit geometric distortions such as translational offsets, rotational deviations, or local deformations, yet they remain valuable due to their structured organization and metadata content. To enhance geometric fidelity while preserving semantic structure, we propose a practical framework for non-rigid polygon registration that adjusts the geometry of cadastral footprints toward LiDAR-derived targets. The framework consists of two core components: (1) establishing correspondences between source and target polygons, and (2) minimizing a robust distance function that governs the registration process. Three deformation models are introduced: a rigid model allowing translations only, a semi-rigid model allowing deformations while keeping the overall structure of source footprints, and a non-rigid model allowing rotations. We evaluate our method by aligning real cadastral datasets to aerial LiDAR data. The results confirm the effectiveness and robustness of the proposed framework in the context of 2D polygonal cadastral data. This work thus represents the first practical solution for non-rigid polygon registration in this domain.

1. Introduction

The rapid evolution of remote sensing technologies has greatly improved the precision and coverage of geospatial data acquisition. Recent nationwide LiDAR surveys provide high-density and up-to-date information that enables numerous applications, including natural hazard monitoring, digital twin generation, 3D building modeling, and urban planning. [1] LiDAR data offer precise geometric information that enhances the accuracy and consistency of geospatial datasets. In building reconstruction, particularly for LoD2 models, ensuring geometric coherence between LiDAR and vector data is essential. Many works have addressed vector data registration to improve spatial alignment between heterogeneous datasets (Biber and Straßer, 2003, Zhu et al., 2020). However, differences in acquisition methods often lead to discrepancies in position, orientation, and shape when compared to highly accurate LiDAR data. This paper focuses on the registration of 2D vector *source* and *target* data. The source data represent building footprints derived from diverse production pipelines, such as cadastral surveys, aerial photogrammetric restitution, or automated extraction workflows. These footprints contain valuable structural information but may not reflect current conditions. Target data are extracted from classified LiDAR data, offering higher geometric fidelity and temporal accuracy. We propose three registration methods minimizing a robust point-to-line distance between source and target footprints, differing by their deformation models: rigid (translation per footprint), non-rigid (vertex-based displacement), and semi-rigid (edge-normal translation).

[1] `https://geoservices.ign.fr/Lidarhd`

Although presented for footprints, the method applies to any 2D polygonal datasets, with or without holes. Figure 1 presents the proposed global pipeline for footprint registration based on rigid, non-rigid and semi-rigid deformation.

2. Related Work

Footprint registration and extraction are key tasks in urban modelling and map updating using archival maps, vector data, DSMs, and LiDAR point clouds.

2.1 Vector and Raster Registration

ICP (Besl and McKay, 1992) remains a standard for rigid vector registration, with geospatial adaptations (Xu et al., 2024, Vaienti et al., 2025), fast robust variants (He et al., 2017, Pomerleau et al., 2013), and non-rigid extensions (Monnier et al., 2013). Vector to raster registration has also been addressed for imagery and historical maps (Tanguy et al., 2020, McKee and Laverdiere, 2021, Yan et al., 2017), while (Djahel et al., 2021) proposes a planar polygon-based method for LiDAR scan registration.

Among stronger baselines, GICP (Segal et al., 2009) is relevant for rigid alignment after boundary sampling, but it is not designed for structured 2D footprints with explicit topology and one to many correspondences. CPD (Myronenko and Song, 2010) and non-rigid ICP variants (Monnier et al., 2013) are also relevant after sampling, but they operate on point sets and do not explicitly preserve topology, edge orientation, or rectilinear structure. TPS and rubber sheeting (Bookstein, 1989) are

This contribution has been peer-reviewed. The double-blind peer-review was conducted on the basis of the full paper.
https://doi.org/10.5194/isprs-annals-XI-1-2026-193-2026

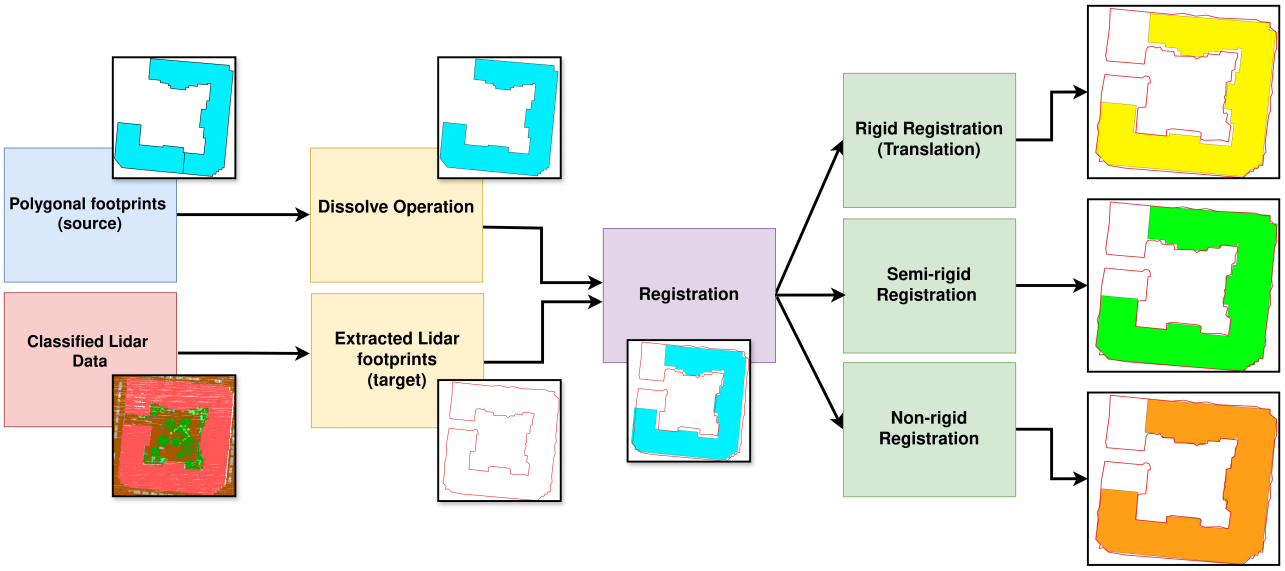

Figure 1. Registration pipeline between source (blue) and target (red) footprints. Depending on the chosen strategy, a rigid registration (translation) can be used for coarse registration, then a non-rigid (rotational) or semi-rigid (rectilinear) registration for refinement.

generic smooth deformation baselines, yet are not well suited to sharp rectilinear footprints. Polygon conflation methods (Ledoux and Arroyo Ohori, 2017) are also related, but often assume pre-matched objects or map fusion settings, making direct comparison less straightforward.

2.2 Building Footprint Extraction From Point Clouds

From DSMs (Brédif et al., 2013, Zhou, 2017), extraction combines parametric shape detection and global optimization. Direct LiDAR based methods (Xu et al., 2015, Rottensteiner and Briese, 2003, Ojogbane et al., 2021, Matikainen et al., 2003) rely on filtering, segmentation, and classification, while robust delineation and regularization refine footprints through graph optimization and geometric constraints (Hui et al., 2021, Awrangjeb and Lu, 2014).

2.3 Deep Learning-Based Building Footprint Extraction

Recent methods combine CNN or YOLO segmentation with polygon regularization (Bauchet et al., 2021, Wei et al., 2019, Sohan et al., 2024). Earlier work uses multi-view imagery (Nex et al., 2013), while DeepFrame and frame field learning produce topologically consistent contours (Li et al., 2021, Girard et al., 2021). For registration, (Zampieri et al., 2018) predicts non-rigid deformations with a multiscale CNN, and (Girard et al., 2018) extends this to joint cadastral alignment and new building detection. In point clouds, (Figueiredo et al., 2021) combines PointNet++ and PCA for 3D CAD model registration (Qi et al., 2017).

Our work builds on these studies by integrating high resolution LiDAR into a two stage pipeline combining association with rigid, semi-rigid, and non-rigid deformation.

3. Proposed Method

In this section, we present three registration methods for registering source to target polygons. Our pipeline consists of data preprocessing followed three methods of registration. The main steps of the framework are the following :

1. **Association**: We begin by establishing correspondences between each source polygon and its corresponding target polygon. The target classified LiDAR point cloud is transformed to target polygons via rasterization and morphological operations. This association step ensures that each source data are reliably linked to their counterpart in the target polygon. Once polygons are associated, point to line correspondences are computed between points sampled on the target footprints and the closest segments of the corresponding source polygon.

2. **Deformation**: We perform registration by looking for a deformation minimizing a combination of a robust distance defined over all point to line correspondences and a data attachment term. This deformation can be of three types: rigid, which register the polygon by translation only, semi-rigid, which deforms the polygon while keeping its rectilinear aspect and non-rigid registration allowing rotations while deforming the polygon.

3.1 Input data

In our experiments, the source data are building footprints from the French BD-TOPO, a comprehensive open dataset containing vector-based descriptions of the French territory and its infrastructure. It offers metric precision suitable for scales ranging from 1:2,000 to 1:50,000. This dataset provides a detailed and consistent representation of geographic and administrative entities across the entire national territory. The target footprints are extracted from LiDAR HD classified point clouds. The French LiDAR HD program, lead by the National Institute of Geographic and Forest Information (IGN) produces and openly distributes a 3D LiDAR scan of the entire surface of French metropolitan territory (and Corsica). The dataset is composed of point clouds cut in $1km^2$ tiles with at least 10 points per m^2 and decimetric accuracy. The 3D point clouds collected through the LiDAR HD program are classified into several classes, including ground, water, low and high vegetation, buildings, bridges, and clutter. Data are open-access and

can be accessed through the links [2] and [3]. In this work, we use only the data associated with the city of Lyon, along with a handcrafted ground trut (not open). That ground truth was created manually by geospatial annotation experts on top of the LiDAR, making sure to also capture inner separations within blocks of buildings. The annotation pipeline includes a quality control step to make sure the final annotations correspond to the specs. Figure 3 presents detailed visualization of the LiDAR data and the corresponding source footprints from the city of Lyon.

3.2 Preprocessing

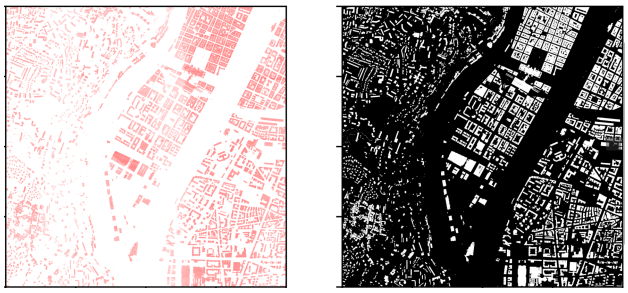

Figure 2. Left: Rasterized LiDAR data. Right: Binary mask

In this paper, we apply our non rigid registration framework to enhance building footprints. Source polygons are building footprints from an existing topographic database, preprocessed with a simple dissolve operation grouping adjacent polygons. This is optional, but if not done, we cannot guarantee that building adjacencies will be preserved. Target polygons are building footprints extracted from classified aerial LiDAR using a rasterization of only the LiDAR points classified as buildings with a pixel size of 30 cm, adapted to the 10 points per m^2 density of the points cloud. Subsequently, we perform morphological opening and closing to regularise the building mask (Figure 2). The Marching Squares algorithm is then used to find the contours of the regularized binary image. Finally, the detected contours are simplified using the Douglas-Peucker algorithm to reduce the number of points while preserving the shape of the contours. Figure 2 shows the rasterized LiDAR (buildings class only) plus the subsequent mask for footprints.

3.3 Polygon association

We now need to associate source to target polygons, which is represented by a bipartite graph $G = (V, E)$ consisting of two disjoint and independent sets of vertices, V_S (source polygons) and V_T (target polygons), such that every edge $e \in E$ connects a vertex in V_T to a vertex in V_S.

The association between each source and target polygons is determined using the Intersection over Minimum (IoM) metric, defined as:

$$\text{IoM}(P_1, P_2) = \frac{\text{Area}(P_1 \cap P_2)}{\min(\text{Area}(P_1), \text{Area}(P_2))} \tag{1}$$

where P_1 and P_2 are the polygons from the source and target datasets, respectively. The IoM metric measures the degree of overlap between two polygons, normalized by the area of the smaller polygon, such that it is 1 if a polygon is included in the other. An association is considered valid if the IoM value exceeds 50%, ensuring the majority of the smallest polygon is overlapped by the largest. This threshold is critical for maintaining accurate correspondences in the registration process. Figure 4 shows the outlines of the resulting building footprints extracted from LiDAR, overlaid with the source footprints.

3.4 Robust distance

Our registration method relies on finding a deformation $M : \mathbb{R}^2 \to \mathbb{R}^2$ minimizing a robust distance with 3 different deformation models. We now define this robust distance which is based on associating the deformed target points $M(A_i^j)$ (sampled every $\delta = 0.15\,\text{m}$ along target edges T_j) to the closest source edge S_k, or equivalently to the projection P_i^j of $M(A_i^j)$ onto the supporting line of S_k:

$$D_{robust}(M) = \sum_{i,j} W_i^j \left(\mathbf{n}_k \cdot \left(P_i^j - M(A_i^j)\right)\right)^2 \tag{2}$$

where $\mathbf{n}_k$ is the normal of S_k and W_i^j is a weight combining distance and angle compatibility:

$$W_i^j = max\left(0, 1 - \left(\frac{|\theta_i^j|}{2 \cdot \theta_{\text{max}}}\right) - \left(\frac{d_i^j}{2 \cdot d_{\text{max}}}\right)\right) \tag{3}$$

where d_i^j is the distance from target sample A_i^j to closest source edge S_k and θ_i^j the angle between source edge T_j and S_k. The weight of associations decreases as the points are further away and as the angles between corresponding source and target edges increases, and only associations for which the distance is below d_{max} and for which edges form an angle below θ_{max} are kept. Figure 5 depicts a scenario of respected pairings with angular compatibility vs without. In our experiments, we used $\theta_{\text{max}} = \frac{\pi}{4}$ and $d_{\text{max}} = 3\,\text{m}$

In addition to the robust distance (2), we can add a data attachment term:

$$D_{attach}(M) = \sum_{i,j} ||M(A_i^j) - A_i^j||^2 \tag{4}$$

3.5 Deformation models

We propose 3 deformation models to parameterize the deformation M of our polygons:

- Rigid deformation: $M(T_K)$ is defined by a translation $T_k \in \mathbb{R}^2$ for each source **polygon** F_k
- Semi-rigid deformation: $M(o_k)$ is defined by an offset o_k defined for each source **edge** S_k of each polygon F_k, meaning that the supporting line of S_k will be translated by $o_k \mathbf{n}_k$
- Non-rigid deformation: $M(T_k^i)$ is defined by a translation T_k^i for each source **vertex** s_i^k of each polygon F_k

3.6 Registration

Registration can now be defined as the process of finding the deformation M that minimises

$$D(M) = D_{\text{robust}}(M) + \alpha\, D_{\text{attach}}(M) \tag{5}$$

[2] https://geoservices.ign.fr/telechargement-api/LiDARHD-NUALID
[3] https://geoservices.ign.fr/telechargement-api/BDTOPO

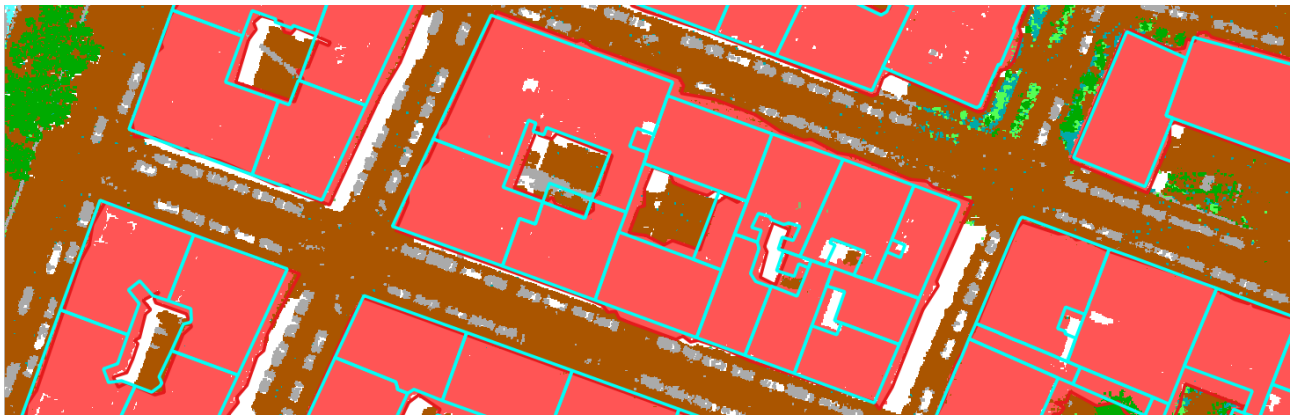

Figure 3. Source footprints (blue) over input classified aerial LiDAR data (red: buildings, green: vegetation, brown: ground) in the city of Lyon.

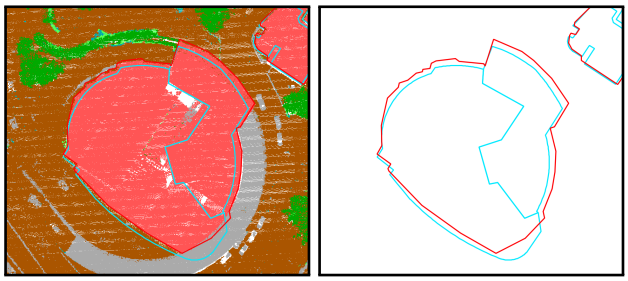

Figure 4. Visualisation of target (red) and source (blue) outlines, showing the extracted and registered building footprints. Discrepancies are visible between the unregistered source and the LiDAR Data.

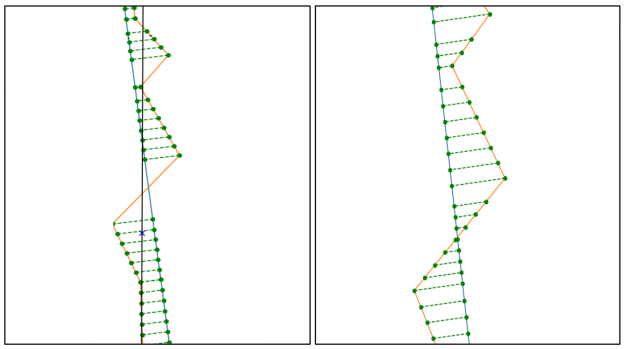

Figure 5. With angular compatibility vs without

3.6.1 Rigid deformation For rigid registration, we don’t need data attachment so the optimal translations T_k are found by nulling the gradient:

$$\nabla_{T_k} D_{robust}(M(T_k)) = 2 \sum_{i,j} W_i^j \mathbf{n}_j \mathbf{n}_j^\top \left(P_i^j + T_k - A_i^j \right) = 0 \tag{6}$$

Solving this system leads to the closed-form solution:

$$T_k = - \left(\sum_j n_j \mathbf{n}_j \mathbf{n}_j^\top \right)^{-1} \sum_j \mathbf{n}_j \mathbf{n}_j^\top \left(\sum_i P_i^j - A_i^j \right) \tag{7}$$

where n_j denotes the number of sampled points assigned to source segment S_j.

3.7 Semi-rigid and Non-rigid Registration

The goal of the semi-rigid and non-rigid registration is to re-estimate the supporting lines of the source polygon segments to improve their fit to the target data. For each source segment with more than two associated sampled points, the supporting line is calculated by weighted least-squares fitting using the weights W_i assigned to each sampled point $\mathbf{P}_i = (x_i, y_i)$.

The weighted centroid $G = (G_x, G_y)$ of the sampled points is:

$$G_x = \frac{\sum_i W_i x_i}{\sum_i W_i}, \quad G_y = \frac{\sum_i W_i y_i}{\sum_i W_i} \tag{8}$$

The deviations of the points from the centroid are:

$$\mathbf{d}_i = \mathbf{P}_i - G, \quad \mathbf{d}_{i,\text{weighted}} = W_i \mathbf{d}_i \tag{9}$$

The covariance matrix M is constructed as:

$$M = \sum_i \mathbf{d}_i \mathbf{d}_{i,\text{weighted}}^T \tag{10}$$

Eigen-decomposition of M yields eigenvalues λ_r and normalized eigenvectors $\mathbf{u}_r$:

$$M \mathbf{u}_r = \lambda_r \mathbf{u}_r \tag{11}$$

The two deformation modes differ only in the way the direction vector $\mathbf{u}$ of the supporting line is determined. In the semi-rigid mode, $\mathbf{u}$ is preserved from the original segment s_i, preventing it from changing its orientation. Denoting the endpoints of s_i by $s_{i,a}$ and $s_{i,b}$, the direction vector is:

$$\mathbf{u} = \frac{s_{i,b} - s_{i,a}}{\| s_{i,b} - s_{i,a} \|} \tag{12}$$

In the non-rigid mode, $\mathbf{u}$ is re-estimated from the data as the unit eigenvector $\mathbf{u}_{\max}$ associated with the largest eigenvalue of M:

$$\mathbf{u}_{\max} = \arg\max_{\mathbf{u}_r} \lambda_r \tag{13}$$

which allows its orientation to change, thus not respecting the angles of the input footprint. For source segments with two or fewer associated sampled points or segments without pairings, the supporting line is retained as the original segment. Figure 6 illustrates the supporting lines, their gravity centers G, and the pairings from sampled points to the closest source segments.

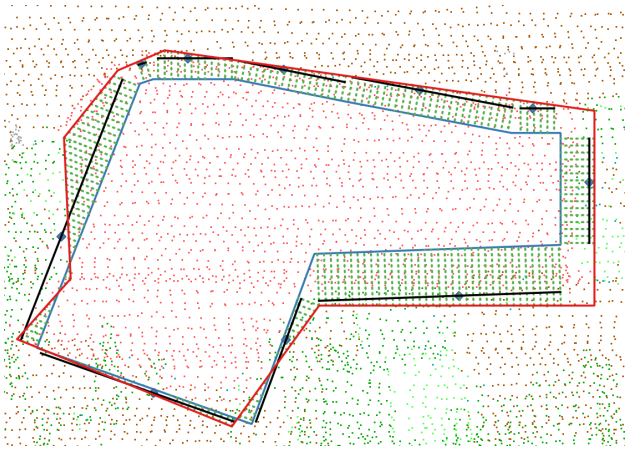

Figure 6. Overview of the generation of supporting lines. Pairings are depicted in green cut lines followed by G points in blue diamonds, then re-estimated lines in black.

3.8 Vertex placement

Ideally, the vertex should be placed at the intersection of supporting lines. However, this proved not robust to some geometric degeneracies. This section explains our strategy to make vertex placement more robust.

3.8.1 Geometric Degeneracy in successive quasi-parallel segments Degenerate configurations can arise particularly in the source polygon, where a straight segment is often subdivided into multiple successive and quasi-parallel segments due to over-segmentation or geometric artifacts. These quasi-parallel divisions, although geometrically close, can lead to instability during the computation of intersections in the deformation process. To address this, we introduce a regularization strategy based on the minimization of a weighted energy function. The objective is to compute an adjusted vertex position $\mathbf{S}'$ that balances the proximity to the supporting lines d_1 and d_2 (from the quasi-parallel source segments), and the fidelity to the original vertex $\mathbf{S}$. The minimization is given by:

$$\mathbf{S}' = \arg\min_{\mathbf{x}} \left(\|\mathbf{x} - d_1\|^2 + \|\mathbf{x} - d_2\|^2 + W \cdot \|\mathbf{x} - \mathbf{S}\|^2 \right) \tag{14}$$

Here, W is a fidelity weight controlling the trade-off between preserving the original geometry and fitting the inferred supporting directions. A small W favours preservation of the source geometry, whereas a larger W biases the result towards registration with the inferred supporting lines.

This minimization problem admits a closed-form solution based on the following system:

$$\begin{aligned} \mathbf{W}_0 &= w \cdot \mathbf{I}_2 + w_1 \cdot \mathbf{n}_1\mathbf{n}_1^\top + w_2 \cdot \mathbf{n}_2\mathbf{n}_2^\top, \\ \mathbf{W}_1 &= w \cdot \mathbf{S} + w_1 \cdot \left(\mathbf{n}_1\mathbf{n}_1^\top \mathbf{p}_1\right) + w_2 \cdot \left(\mathbf{n}_2\mathbf{n}_2^\top \mathbf{p}_2\right), \\ \mathbf{S}' &= \left(\mathbf{W}_0 + \varepsilon \cdot \mathbf{I}_2\right)^{-1} \mathbf{W}_1 \end{aligned} \tag{15}$$

where:

- $\mathbf{n}_1$, $\mathbf{n}_2$ are the unit normals of the supporting lines d_1 and d_2,
- $\mathbf{p}_1$, $\mathbf{p}_2$ are any points lying on the supporting lines d_1, d_2,
- w_1, w_2 are the total registration weights of the sampled points associated with d_1, d_2,
- w is the fidelity weight W,
- $\mathbf{I}_2$ is the 2×2 identity matrix,
- ε is a small regularization constant added for numerical stability.

This formulation ensures that even in the presence of quasi-parallel segments in the source polygon, the deformation process remains stable and geometrically coherent.

3.8.2 Handling Residual Self-Intersections Despite the previously introduced geometric constraints and predictive strategies designed to prevent self-intersections, they may still occur in some rare configurations. These typically arise during the non-rigid deformation process when highly entangled or collapsed geometries induce topological inconsistencies.

To mitigate these cases, we introduce a post-processing step that checks whether a given deformed polygon $\mathcal{P}$ can be partitioned into multiple disjoint simple polygons due to self-intersection. Let:

$$\{\mathcal{P}_1, \mathcal{P}_2, \ldots, \mathcal{P}_n\} = \text{Fragment}(\mathcal{P}) \tag{16}$$

denote the set of n simple, non-intersecting polygons resulting from a fragmentation operation applied to the self-intersecting polygon $\mathcal{P}$. We then retain only the polygon with the largest area:

$$\mathcal{P}^{\text{final}} = \arg\max_{\mathcal{P}_i} \left(\text{Area}(\mathcal{P}_i)\right), \quad \text{for } i \in \{1, 2, \ldots, n\} \tag{17}$$

This approach ensures the resulting geometry is valid, topologically consistent, and preserves the dominant structural component of the polygon.

In practice, this operation acts as a safeguard against degenerate configurations and has proven effective in eliminating the residual cases of self-intersections not captured by earlier registration constraints.

https://doi.org/10.5194/isprs-annals-XI-1-2026-193-2026

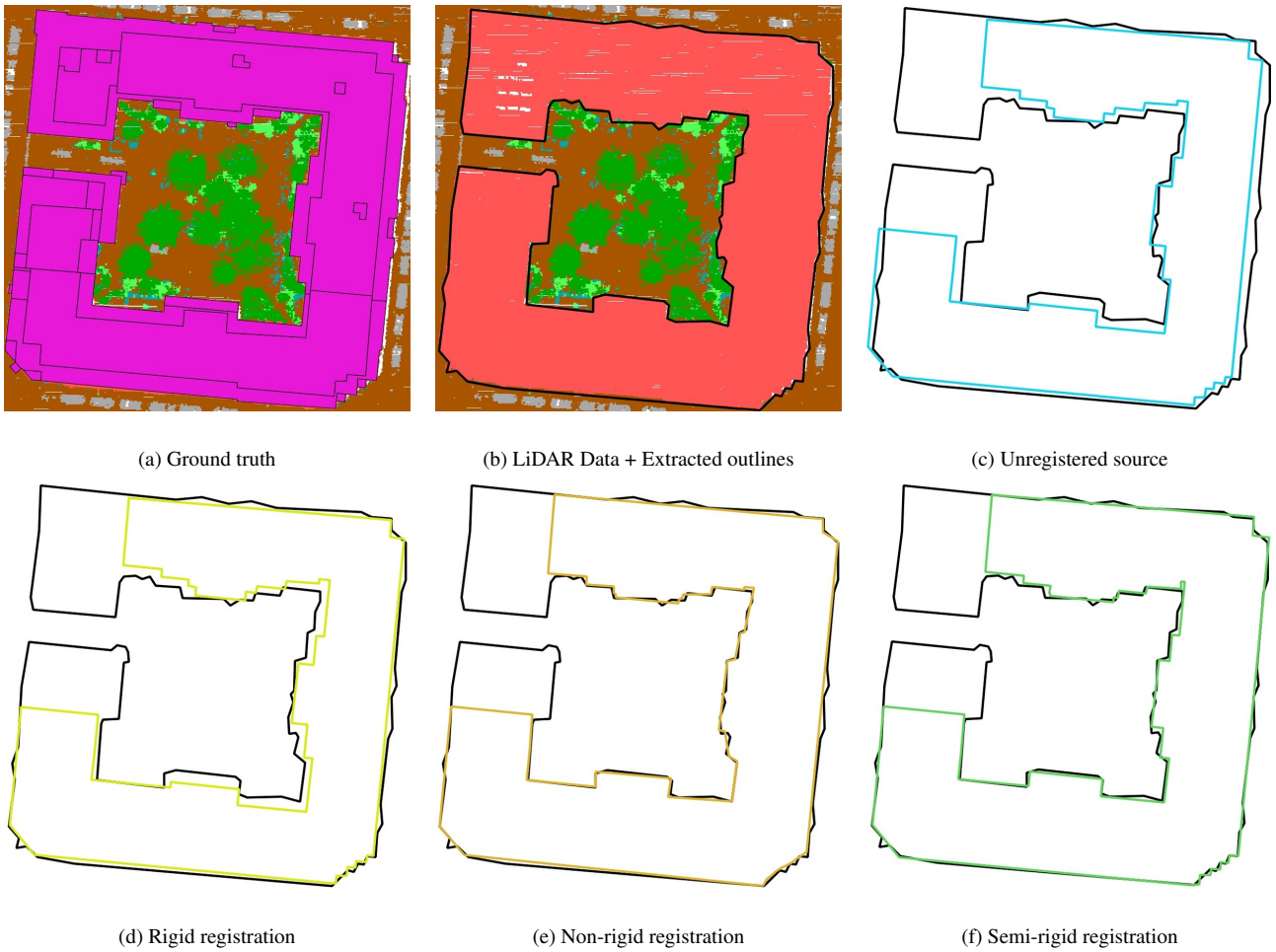

(a) Ground truth (b) LiDAR Data + Extracted outlines (c) Unregistered source

(d) Rigid registration (e) Non-rigid registration (f) Semi-rigid registration

Figure 7. Visual comparison of registration strategies for building footprints. Rows 1 shows : (a–b-c) ground truth and LiDAR data plus the unregistered source data Row 2 shows : (d-e-f) rigid registration result (translation only), non-rigid and semi-rigid registration. Both deformation methods (non-rigid, semi-rigid) are applied after rigid registration.

4. Experiments

To evaluate our registration framework, we performed experiments on a test area extracted from the city of Lyon (France). Results are analysed both qualitatively and quantitatively.

4.1 Qualitative Evaluation

Figure 7 illustrates the progressive improvement in geometric consistency between the source data and the target data across the different registration stages. The first row presents the reference data: manual ground truths, which serve only for comparison purposes in section 4.2, plus the LiDAR-based target polygons displayed as red outlines. The second row show the unregistered dissolved source data and the result of the rigid registration, which primarily corrects global shifts with a translation. The third row displays the final deformation stages: the non-rigid registration, providing maximal local adaptability to rotational discrepancies, and the semi-rigid model, which balances flexibility and structural regularity for a more stable reconstruction. The difference between non-rigid and semi-rigid registration is mostly visible in the corners for given the example.

4.2 Quantitative Evaluation

We apply four complementary metrics to evaluate both geometric proximity and directional consistency between the registered and reference polygons. Two metrics are expressed in meters and relate to contour distances, while the other two are in degrees and reflect angular deviations. In all cases, lower values indicate better registration performance.

- **Contour Precision (m)**: Average shortest distance from each segment in the aligned polygon to the closest segment in the reference polygon.
- **Contour Recall (m)**: Average shortest distance from each segment in the reference polygon to the closest segment in the aligned polygon.
- **Orientation Precision** (°): Average angular deviation between corresponding segments in the aligned and reference polygons.
- **Orientation Recall** (°): Average angular deviation from reference segments to their closest aligned counterparts.

These metrics are summarized in Table 1, comparing the unregistered source polygons, the rigid registration, the semi-rigid model, and the non-rigid registration against manual ground truth data. Results are reported for four correspondence categories: one-to-one (1–1), many-to-one (N–1), one-to-many (1–M), and many-to-many (N–M).

This contribution has been peer-reviewed. The double-blind peer-review was conducted on the basis of the full paper.
https://doi.org/10.5194/isprs-annals-XI-1-2026-193-2026 | © Author(s) 2026. CC BY 4.0 License.

Category	C_prec (m)	C_rec (m)	O_prec (°)	O_rec (°)
Unregistered source vs. ground truth				
1–1	2.05	1.18	12.45	12.42
N–1	1.63	1.29	**18.04**	14.97
1–M	2.68	2.84	18.18	24.25
N–M	1.12	1.30	18.89	18.98
Rigid registration vs. ground truth				
1–1	**1.98**	**1.12**	**11.95**	**12.02**
N–1	**1.60**	**1.27**	18.08	**14.81**
1–M	**2.64**	**2.67**	**17.97**	**23.94**
N–M	**1.02**	**1.33**	**17.70**	**18.94**
Semi-rigid registration vs. ground truth				
1–1	**1.69**	**0.83**	**10.62**	**10.66**
N–1	**1.27**	1.11	**15.99**	**13.50**
1–M	**0.90**	**3.73**	**12.34**	**23.45**
N–M	3.20	**1.97**	19.26	22.76
Non-rigid registration vs. ground truth				
1–1	1.71	0.83	11.01	11.07
N–1	1.19	**0.97**	16.62	14.04
1–M	2.21	3.37	15.63	22.96
N–M	**0.72**	3.06	**14.96**	**19.13**
Semi-rigid (no rigid preprocessing) vs. ground truth				
1–1	**1.68**	0.83	10.66	10.68
N–1	1.52	1.11	16.22	13.52
1–M	**0.87**	4.07	11.42	23.15
N–M	**3.18**	**1.94**	**18.95**	23.20
Non-rigid (no rigid preprocessing) vs. ground truth				
1–1	1.72	0.84	11.02	11.08
N–1	1.20	0.97	16.62	14.04
1–M	2.22	3.38	15.63	22.96
N–M	0.72	3.07	14.97	19.13

Table 1. Quantitative comparison between source and ground truth building footprints across registration variants. Bold values indicate superior performance relative to the preceding model.

Rigid registration markedly improves geometric proximity compared to unregistered data. Deformable models refine results further: the semi-rigid model achieves the best overall contour precision, while the non-rigid variant adapts better to complex (N–M) configurations.

The results in Table 1 reveal substantial improvements when deformable registration is applied. Both rigid and semi-rigid strategies outperform the unregistered data, especially in simpler correspondences (1–1, N–1). The semi-rigid model yields the best contour precision and angular coherence, while the non-rigid model excels in more complex many-to-many relationships, albeit with slightly less regular contours.

Furthermore, Table 1 also presents the results obtained without the rigid registration step. Compared with the rigid-preprocessed variants, rigid initialization generally improves both contour and orientation stability for the two deformation models.

For the semi-rigid model, the rigid step enhances contour recall and angular precision, especially in the 1–1 and N–1 categories. Without it, performance slightly decreases, particularly in multi-object cases.

For the non-rigid model, the absence of rigid initialization keeps results close but leads to higher errors in fragmented configurations. The rigid-initialized version achieves better coherence and lower deformation errors. In practice, the rigid phase can be considered optional for already well-aligned data and particularly useful for correcting large initial discrepancies.

Furthermore, semi-rigid registration provides the most consistent improvements across all categories, maintaining structural regularity while achieving accurate spatial and angular fits. The non-rigid model remains advantageous in highly fragmented urban patterns.

Finally, The study area over Lyon contains 18,979 ground-truth undissolved footprints, 2,738 dissolved ground-truth footprints, and 3,039 dissolved source footprints. The full pipeline was executed on a Dell laptop equipped with a 10th generation Intel Core i9 processor in about 1,800 s for the Lyon region. Since the method operates footprint by footprint, it does not raise major scalability issues.

5. Conclusions and Perspectives

In this work, we proposed three registration strategies to improve the geometric accuracy of building footprints by registering them with LiDAR-derived data. Experimental results demonstrate clear improvements in both both contour and orientation accuracy compared to the source footprints. Among the tested strategies, the semi-rigid and non-rigid models achieve superior performance over the rigid registration, offering accurate and better results.

Perspective. As a continuation of this work, we are developing a method that takes into account inter-building adjacency relationships during registration. By incorporating spatial context across neighboring buildings, we aim to enhance geometric regularity, reduce alignment artifacts at shared boundaries, and better handle dense urban configurations. This extension will further improve the topological consistency and structural integrity of the registered building layers.

References

Awrangjeb, M., Lu, G., 2014. Automatic building footprint extraction and regularisation from lidar point cloud data. *2014 International Conference on Digital Image Computing: Techniques and Applications (DICTA)*, IEEE, 1–8.

Bauchet, J.-P., Mapurisa, W., Gobbin, A., Tripodi, S., Tarabalka, Y., Duan, L., Laurore, L., 2021. Rooftops or footprints? reliable building footprint extraction from high-resolution satellite images. *2021 IEEE International Geoscience and Remote Sensing Symposium IGARSS*, IEEE, 274–277.

Besl, P. J., McKay, N. D., 1992. Method for registration of 3-d shapes. *Sensor fusion IV: control paradigms and data structures*, 1611, Spie, 586–606.

Biber, P., Straßer, W., 2003. The normal distributions transform: A new approach to laser scan matching. *Proceedings 2003 IEEE/RSJ International Conference on Intelligent Robots and Systems (IROS 2003)(Cat. No. 03CH37453)*, 3, IEEE, 2743–2748.

Bookstein, F. L., 1989. Principal Warps: Thin-Plate Splines and the Decomposition of Deformations. *IEEE Transactions on Pattern Analysis and Machine Intelligence*, 11(6), 567–585.

Brédif, M., Tournaire, O., Vallet, B., Champion, N., 2013. Extracting polygonal building footprints from digital surface models: A fully-automatic global optimization framework. *ISPRS journal of photogrammetry and remote sensing*, 77, 57–65.

Djahel, R., Monasse, P., Vallet, B., 2021. Towards efficient indoor/outdoor registration using planar polygons. *XXIV ISPRS Congress*, 2, 51–58.

Figueiredo, L., Ivson, P., Celes, W., 2021. Deep learning-based framework for Shape Instance Registration on 3D CAD models. *Computers & Graphics*, 101, 72–81.

Girard, N., Charpiat, G., Tarabalka, Y., 2018. Aligning and updating cadaster maps with aerial images by multi-task, multi-resolution deep learning. *Asian Conference on Computer Vision*, Springer, 675–690.

Girard, N., Smirnov, D., Solomon, J., Tarabalka, Y., 2021. Polygonal building extraction by frame field learning. *Proceedings of the IEEE/CVF Conference on Computer Vision and Pattern Recognition*, 5891–5900.

He, Y., Liang, B., Yang, J., Li, S., He, J., 2017. An iterative closest points algorithm for registration of 3D laser scanner point clouds with geometric features. *Sensors*, 17(8), 1862.

Hui, Z., Li, Z., Cheng, P., Ziggah, Y. Y., Fan, J., 2021. Building extraction from airborne LiDAR data based on multi-constraints graph segmentation. *Remote Sensing*, 13(18), 3766.

Ledoux, H., Arroyo Ohori, K., 2017. Solving the Horizontal Conflation Problem with a Constrained Delaunay Triangulation. *Journal of Geographical Systems*, 19(1), 21–42.

Li, Z., Xin, Q., Sun, Y., Cao, M., 2021. A deep learning-based framework for automated extraction of building footprint polygons from very high-resolution aerial imagery. *Remote Sensing*, 13(18), 3630.

Matikainen, L., Hyyppä, J., Hyyppä, H., 2003. Automatic detection of buildings from laser scanner data for map updating. *International Archives of Photogrammetry, Remote Sensing and Spatial Information Sciences*, 34(3/W13), 218–224.

McKee, J., Laverdiere, M., 2021. Automated registration of vector data to overhead imagery. *2021 IEEE International Geoscience and Remote Sensing Symposium IGARSS*, IEEE, 5465–5468.

Monnier, F., Vallet, B., Paparoditis, N., Papelard, J.-P., David, N., 2013. Registration of terrestrial mobile laser data on 2D or 3D geographic database by use of a non-rigid ICP approach. *ISPRS Annals of the Photogrammetry, Remote Sensing and Spatial Information Sciences*, 2, 193–198.

Myronenko, A., Song, X., 2010. Point Set Registration: Coherent Point Drift. *IEEE Transactions on Pattern Analysis and Machine Intelligence*, 32(12), 2262–2275.

Nex, F., Rupnik, E., Remondino, F., 2013. Building footprints extraction from oblique imagery. *ISPRS Annals of the Photogrammetry, Remote Sensing and Spatial Information Sciences*, 2, 61–66.

Ojogbane, S. S., Mansor, S., Kalantar, B., Khuzaimah, Z. B., Shafri, H. Z. M., Ueda, N., 2021. Automated building detection from airborne LiDAR and very high-resolution aerial imagery with deep neural network. *Remote Sensing*, 13(23), 4803.

Pomerleau, F., Colas, F., Siegwart, R., Magnenat, S., 2013. Comparing ICP variants on real-world data sets: Open-source library and experimental protocol. *Autonomous robots*, 34(3), 133–148.

Qi, C. R., Yi, L., Su, H., Guibas, L. J., 2017. Pointnet++: Deep hierarchical feature learning on point sets in a metric space. *Advances in neural information processing systems*, 30.

Rottensteiner, F., Briese, C., 2003. Automatic generation of building models from LIDAR data and the integration of aerial images.

Segal, A., Haehnel, D., Thrun, S., 2009. Generalized-icp. *Proceedings of Robotics: Science and Systems V*, Seattle, USA.

Sohan, M., Thotakura, S. R., Reddy, C. V. R., 2024. A review on yolov8 and its advancements. *International Conference on Data Intelligence and Cognitive Informatics*, Springer, Singapore.

Tanguy, Y., Michel, J., Salgues, G., 2020. Automatic registration of vector data with optical images. *The International Archives of the Photogrammetry, Remote Sensing and Spatial Information Sciences*, 43, 191–196.

Vaienti, B., di Lenardo, I., Kaplan, F., 2025. Georeferencing historical maps using local feature matching and Delaunay consistency. *Cartography and Geographic Information Science*, 1–23.

Wei, S., Ji, S., Lu, M., 2019. Toward automatic building footprint delineation from aerial images using CNN and regularization. *IEEE Transactions on Geoscience and Remote Sensing*, 58(3), 2178–2189.

Xu, S., Vosselman, G., Oude Elberink, S., 2015. Detection and classification of changes in buildings from airborne laser scanning data. *Remote sensing*, 7(12), 17051–17076.

Xu, Y., Li, J., Xie, X., Xie, Z., 2024. Matching the building footprints of different vector spatial datasets at a similar scale based on one-class support vector machines. *International Journal of Geographical Information Science*, 38(8), 1555–1582.

Yan, W. Y., Easa, S. M., Shaker, A., 2017. Polygon-based image registration: A new approach for geo-referencing historical maps. *Remote Sensing Letters*, 8(7), 703–712.

Zampieri, A., Charpiat, G., Girard, N., Tarabalka, Y., 2018. Multimodal image alignment through a multiscale chain of neural networks with application to remote sensing. *Proceedings of the European Conference on Computer Vision (ECCV)*, 657–673.

Zhou, Q., 2017. Digital elevation model and digital surface model. *International encyclopedia of geography: People, the earth, environment and technology*, 1–17.

Zhu, B., Ye, Y., Yang, C., Zhou, L., Liu, H., Cao, Y., 2020. Fast and robust registration of aerial images and lidar data based on structrual features and 3d phase correlation. *arXiv preprint arXiv:2004.09811*.